

# Effect of Hf on microstructure and creep properties of a hot corrosion resistant nickel-based single crystal superalloy

Li Ma<sup>1,2</sup>, \*Dong Wang<sup>2</sup>, Gong Zhang<sup>2</sup>, Jian Shen<sup>2</sup>, and \*\*Jian Zhang<sup>2</sup>

1. School of Materials Science and Engineering, Northeastern University, Shenyang 110089, China

2. Shi-changxu Innovation Center for Advanced Materials, Institute of Metal Research, Chinese Academy of Sciences, Shenyang 110016, China

Copyright © 2025 Foundry Journal Agency

**Abstract:** To investigate the microstructure and creep properties of a hot corrosion resistant Ni-based single crystal superalloy containing different hafnium (Hf) additions (0–0.4wt.%), creep test was performed at 980 °C/200 MPa. Optical microscopy, scanning electron microscopy, electron probe micro analysis (EPMA), and transmission electron microscopy were employed to analyze the microstructure differences. With the increase of Hf, the creep rupture life of the alloys at 980 °C/200 MPa gradually increases. Microstructure analysis reveals that Hf promotes the transformation of carbide morphology from script to rod-like and finally to blocky. Upon the addition of Hf, there is an increase in the volume fraction of blocky MC carbides, along with an elevation in the partitioning ratio of Cr and Mo elements. Concurrently, the  $\gamma/\gamma'$  interfacial dislocation spacing undergoes a reduction. It is found that script carbides are more likely to cause stress concentration in high temperature creep, leading to nucleation and propagation of microcracks. The formation mechanism of blocky MC carbides is related to the increase in precipitation temperature and lattice constant, and its beneficial impact on creep resistance is also investigated based on the analysis of the creep test results.

**Keywords:** Ni-based single crystal superalloys; hafnium; creep properties; MC carbides; hot corrosion resistance

CLC numbers: TG146.1<sup>1</sup>5

Document code: A

Article ID: 1672-6421(2025)02-173-09

## 1 Introduction

Nickel-based single crystal (SX) superalloys are widely used as blades and vanes in advanced aviation turbine engines and industrial gas turbines (IGTs) due to their excellent high-temperature performances such as high creep resistance, fatigue resistance, and corrosion resistance<sup>[1-3]</sup>. However, during the casting of these SX components, especially large-sized IGT blades, there is a high probability of inducing grain boundaries (GBs) defects. As a result, manufacturing cost of the blades

is high due to high scrap rates<sup>[4,5]</sup>. The deformation induced by creep is one of the dominant failure modes during the service life of turbine blades<sup>[2,6]</sup>. The existence of grain boundary defects accelerates the formation of creep cracks and drastically degrades the creep properties of SX superalloys. Therefore, in some alloys, minor elements such as carbon (C), boron (B), and hafnium (Hf) are introduced to make the superalloys more resistant to problems associated with grain boundary defects. The objective is to balance safe service performance and manufacturing costs<sup>[7-11]</sup>.

Compared to C and B, there is relatively less research on the effect of Hf on the mechanical properties of SX superalloys. Particularly, the impact of the interaction between Hf and both C and B on the microstructure and mechanical properties of hot corrosion resistant nickel-based SX superalloys is seldom reported. Shi et al.<sup>[12]</sup> reported that a longer stress rupture life was achieved at 1,100 °C/140 MPa due to the reduction of interdendrite  $\gamma'$  size and a low amount of residual eutectics by addition of a moderate amount

### \*Dong Wang

Male, born in 1983, Professor. Research interests: directional solidification and single crystal superalloys.

E-mail: dwang@imr.ac.cn

### \*\*Jian Zhang

Male, born in 1972, Professor, Doctoral Supervisor. Research interests: directional solidification and single crystal superalloys.

E-mail: jianzhang@imr.ac.cn

Received: 2024-06-04; Revised: 2024-08-19; Accepted: 2024-12-09

of Hf in DD6 alloy. Zhao et al. [13] reported that a longer creep rupture life was obtained at 1,100 °C/130 MPa with addition of 0.4wt.% Hf in a C-containing DD11 alloy, which was attributed to the increase of  $\gamma/\gamma'$  misfit and the solution strengthening effect. However, it was reported that shorter creep lives were obtained at 950 °C/210 MPa and 950 °C/290 MPa due to detrimental influence of eutectics containing large and irregular  $\gamma'$  by addition of C, B, and Hf in RR2072 alloy [14]. Kong et al. [15] also reported that higher creep rates during the primary and secondary creep stages were observed at 950 °C/210 MPa and 1,050 °C/165 MPa due to detrimental influence of interdendritic regions that contained large, irregular and partially rafted  $\gamma'$  particles and brittle MC carbides by addition of C, B and Hf in RR2086 alloy.

Analysis shows that Hf is a significant carbide forming element, and its addition tends to increase the carbides content and promote the precipitation of blocky carbides [14, 16, 17], while the quantity and morphology of carbides are closely related to crack initiation and alloy properties. For example, it is reported that microcracks preferentially nucleate and propagate near the script MC carbides rather than blocky carbides [16]. However, the local stress and strain generated during creep loading near the carbides with different morphologies have rarely been reported. In addition to the effect on quantity and morphology of carbides, Hf reduces the volume fraction of micropores because carbides fill the shrinkage of micropores in the later stages of solidification [18], promoting the formation of eutectics [19]. Therefore, the effect of Hf on creep could be a trade-off. On one hand, fewer micropores and modified carbide morphology benefit the creep property. On the other hand, solution heat treatment becomes challenging when there is a large volume fraction of eutectics in the as-cast alloys. A less homogenized microstructure is detrimental to creep.

In this study, a corrosion resistant nickel-based SX superalloy

was used as the master alloy. Various concentrations of Hf ranging from 0 to 0.4wt.% were introduced into the master alloy. A comprehensive comparison of the microstructure of the experimental superalloys in both the as-cast and heat-treated states was conducted. Subsequently, creep tests were conducted at 980 °C/200 MPa to assess the influence of Hf on high temperature creep properties of the experimental superalloys. The objective of this study was to optimize the Hf addition in nickel-based SX superalloys, so as to provide insights that could enhance the mechanical properties of these superalloys.

## 2 Experimental procedures

The base alloy investigated in this study was a corrosion resistant nickel-based SX superalloy, with the nominal composition (in wt.%) of 12.5% Cr, 4.5% Co, 3.8% Al, 0.5% Mo, 5% W, 5.5% Ta, 4% Ti, 0.05% C, 0.005% B, and Ni is the balance. Three SX slabs with dimensions of 20 mm×80 mm×220 mm and containing various Hf content (0, 0.2wt.%, and 0.4wt.%, referred to as 0 Hf, 0.2 Hf, and 0.4 Hf, respectively) were prepared through a high rate solidification (HRS) process. The solution and aging treatment processes of the three experimental alloys, as listed in Table 1, were determined by both the metallurgical analysis and differential scanning calorimetry (DSC). To avoid incipient melting of 0.4 Hf alloy, a pre-solid solution was performed at 1,230 °C for 2 h. After aging treatment, the specimens for creep test were machined. The dimensions of the gauge section was 5 mm in diameter and 25 mm in length. The creep tests were conducted at 980 °C/200 MPa in air with the loading direction parallel to the <001> orientation of the specimens. Deviations from <001> orientation were measured as 2.2°, 4°, and 6.5°, respectively for 0 Hf, 0.2 Hf, and 0.4 Hf alloys. Two creep tests were interrupted in the tertiary creep region at 135 h for 0 Hf alloy and 145 h for 0.2 Hf alloy, respectively.

Table 1: Solution and aging heat treatment of three experimental alloys

Alloy	Solution heat treatment	Aging heat treatment
0 Hf	1,250 °C/6 h, air cooling (AC)	1,110 °C/4 h, AC + 870 °C/24 h, AC
0.2 Hf	1,250 °C/6 h, AC	1,110 °C/4 h, AC + 870 °C/24 h, AC
0.4 Hf	1,230 °C/2 h; 1,250 °C/6 h, AC	1,110 °C/4 h, AC + 870 °C/24 h, AC

The cross-sectional microstructures of as-cast and heat-treated alloys perpendicular to <001> were examined. Samples were prepared using standard metallographic techniques and etched using a solution consisting of 20 g CuSO<sub>4</sub>, 100 mL HCl and 80 mL H<sub>2</sub>O. Microstructural examination was performed using an optical microscope (OM) and a Zeiss Supra 55 field-emission scanning electron microscope (FE-SEM). The volume fractions of  $\gamma/\gamma'$  eutectics,  $\gamma'$  precipitates, and carbides were determined using the standard point count method by Photoshop software. Image-Pro software was used for measurement of  $\gamma'$  size,  $\gamma$  channel width, and secondary phase size. To study the crack initiation sites and

the crack propagation character during creep, the ruptured specimens were sectioned parallel to the tensile axis. Polished surfaces were prepared metallographically and observed by backscattered electron imaging and electron backscattered diffraction (EBSD). In addition, the dislocation substructure was analyzed using JEM-2100P transmission electron microscopy (TEM). Foils for TEM were cut from the gauge section perpendicular to the applied stress axis, at a position of 5 mm away from the necked region. These slices were mechanically grounded to 50  $\mu$ m and electro-polished at -30 °C and 20 V in a solution consisting of 10% perchloric acid and 90% ethanol. Dislocation network spacing measurement was

made from images obtained under a <200> type two-beam condition in the [001] zone axis parallel to the g-vectors.

The elemental partitioning ratio of  $\gamma$  and  $\gamma'$  phases,  $k_i$ , is defined as

$$k_i = \frac{C_i^\gamma}{C_i^{\gamma'}} \quad (1)$$

where  $k_i$  represents each of the alloying elements,  $C_i^\gamma$  and  $C_i^{\gamma'}$  correspond to the atomic concentration of element  $i$  within the  $\gamma$  and  $\gamma'$  phases, respectively. A value of  $k_i$  that is greater than or less than 1 indicates that element  $i$  preferentially partitions into the  $\gamma$  or  $\gamma'$  phase, respectively. Concentration profiles of  $\gamma$  and  $\gamma'$  phases were also measured by a TEM with energy dispersive spectrum (EDS). EDS data were collected from both  $\gamma$  and  $\gamma'$  phases in at least five different areas for each

experimental alloy. Values of  $C_i^\gamma$  and  $C_i^{\gamma'}$  were averaged over the multiple measurements taken from different areas.

### 3 Results

#### 3.1 As-cast microstructure

Figure 1 shows the OM microstructures of the as-cast experimental alloys. The microstructures of all the three specimens exhibit a typical dendritic structure. The average primary dendritic arm spacing (PDAS), area fraction of the  $\gamma/\gamma'$  eutectic, and the micropores in the three alloys are compared in Table 2. The PDAS decreases and eutectic content increases significantly with the increase of Hf content. In addition, the area fraction of micropores remarkably decreases to 0.11% in 0.4 Hf alloy. Similar effect of Hf on micropores has also been reported previously<sup>[18]</sup>.

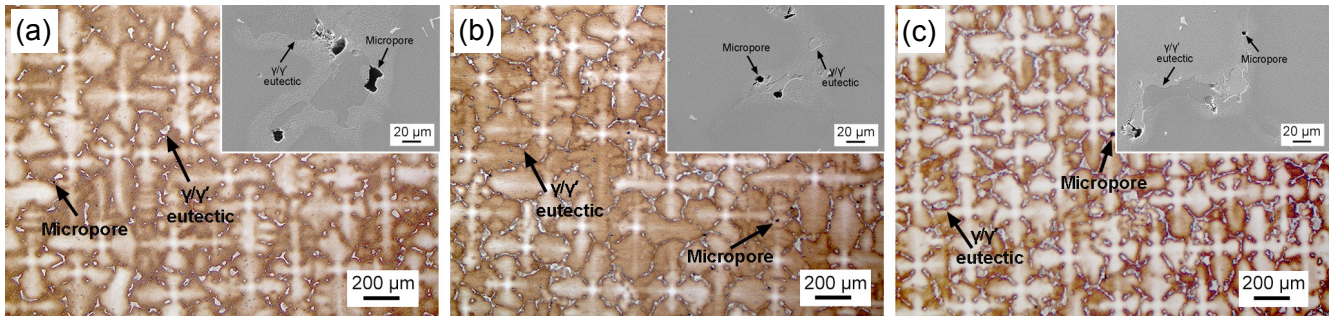


Fig. 1: Dendritic microstructures of as-cast experimental alloys: (a) 0 Hf, (b) 0.2 Hf; (c) 0.4 Hf. Details of micropore and eutectic are shown in the enlarged inserts (SEM)

Table 2: Microstructure characterization of three experimental as-cast alloys

Alloy	PDAS ( $\mu\text{m}$ )	Eutectic (vol.%)	Micropore (vol.%)
0 Hf	401 $\pm$ 33	2.98 $\pm$ 0.45	0.30 $\pm$ 0.12
0.2 Hf	386 $\pm$ 13	3.96 $\pm$ 0.80	0.24 $\pm$ 0.07
0.4 Hf	307 $\pm$ 16	4.81 $\pm$ 0.98	0.11 $\pm$ 0.05

Figure 2 shows the BSE-SEM image of the interdendritic region of the as-cast alloys. The interdendritic region of 0 Hf alloy exhibits mainly eutectics and Ti- and Ta-rich MC carbides. As shown in Figs. 2(b) and (c), in addition to MC carbides and eutectics in the interdendritic region of 0.2 Hf and 0.4 Hf alloys, Hf containing phase (gray-contrast) near the eutectics that has been identified as  $\text{Ni}_5\text{Hf}$  in a previous report<sup>[20]</sup> is observed. As Hf content increases, the volume fraction of  $\text{Ni}_5\text{Hf}$  phase increases. EDS results indicate that  $\text{Ni}_5\text{Hf}$  phase is rich in Ni, Hf, and Ti.

Figure 3 displays the BSE-SEM images of MC carbides in the as-cast alloys. In 0 Hf and 0.2 Hf alloys, the MC carbides exhibit script, rod-like, and blocky morphologies. However, in 0.4 Hf alloy, most of the MC carbides are rod-like and blocky. Figure 4(a) shows the volume fraction of carbides with different morphologies. The results indicate that with an increase in Hf content, the volume fraction of script carbides decreases, while the volume fraction of blocky carbides increases gradually. The

addition of Hf promotes the transformation of the morphology of MC carbides from script to rod-like and finally to blocky. The compositions of script MC carbides and blocky MC carbides were measured using EPMA. In Fig. 4(b), the ratios of the metallic elements in the MC carbides are compared. Blocky MC particles contain significantly higher content of Ti, Ta, and Hf, but less Cr than the script MC carbides.

#### 3.2 Microstructure after heat treatment

Figure 5 shows the typical OM images of heat-treated microstructures of the experimental alloys. It can be seen that with the increase of Hf content, the volume fraction of residual eutectic increases. The average volume fraction of the residual eutectic is 1.16% in 0 Hf alloy and increases to 2.15% in 0.4 Hf alloy.

Figure 6 shows the BSE-SEM images of MC carbides in the heat-treated experimental alloys. In both 0 Hf and 0.2 Hf alloys, the morphology of MC carbides exhibits script, rod-like, and blocky shapes. In contrast, in the 0.4 Hf alloy, the MC carbides exhibit rod-like and blocky morphologies. Therefore, compared to Fig. 3, it can be seen that there is no obvious change of MC carbides after heat treatment.

Figure 7 shows typical  $\gamma'$  morphology of the alloys after heat treatment. The morphology of  $\gamma'$  precipitates is all cubic. The difference in the size of  $\gamma'$  precipitates between the dendrite core and the interdendrite region in the 0 Hf alloy is minimal. However, with the increase of Hf content, the difference in

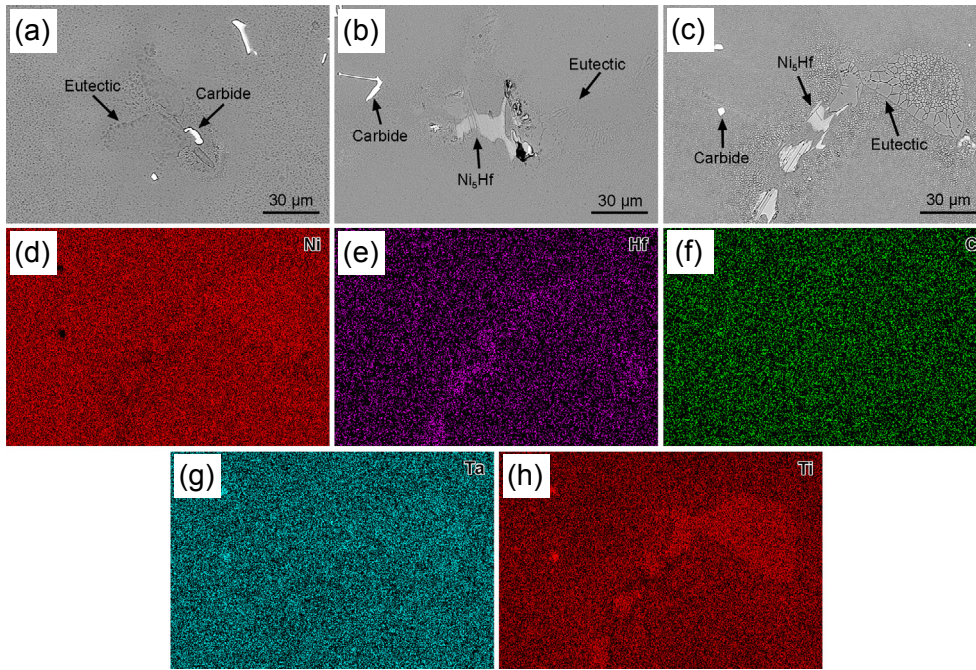


Fig. 2: BSE-SEM images of the interdendrite regions of 0 Hf (a), 0.2 Hf (b), 0.4 Hf (c) alloys, and the corresponding EDS element distribution maps of Ni (d), Hf (e), C (f), Ta (g), and Ti (h) in 0.4 Hf alloy

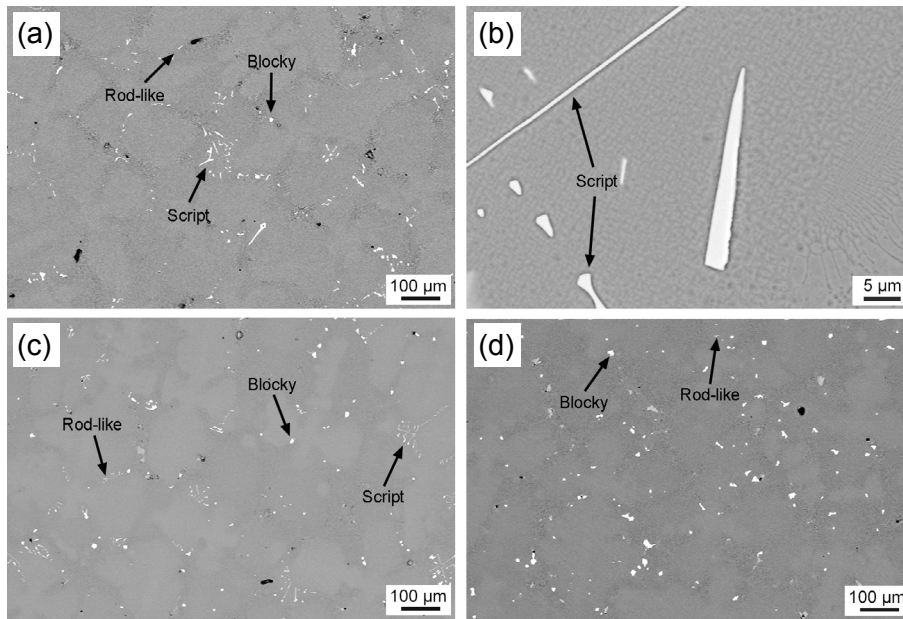


Fig. 3: BSE-SEM images of MC carbides in as-cast alloys: (a) 0 Hf; (b) amplification of script carbide in 0 Hf; (c) 0.2 Hf; and (d) 0.4 Hf alloys

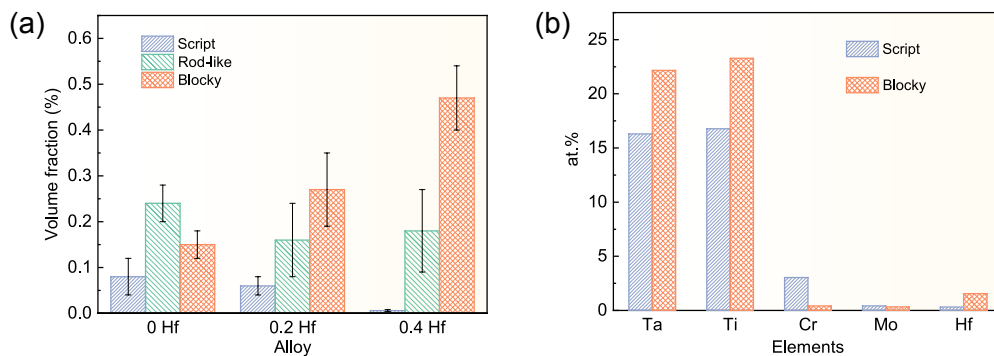


Fig. 4: Volume fraction of carbides with different morphologies (a) and percentages of atoms in MC carbides (b)

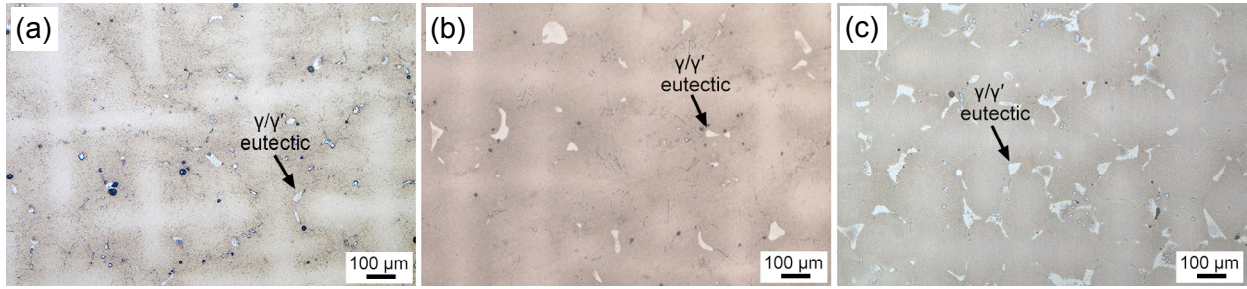


Fig. 5: Microstructures of heat-treated experimental alloys: (a) 0 Hf; (b) 0.2 Hf; and (c) 0.4 Hf

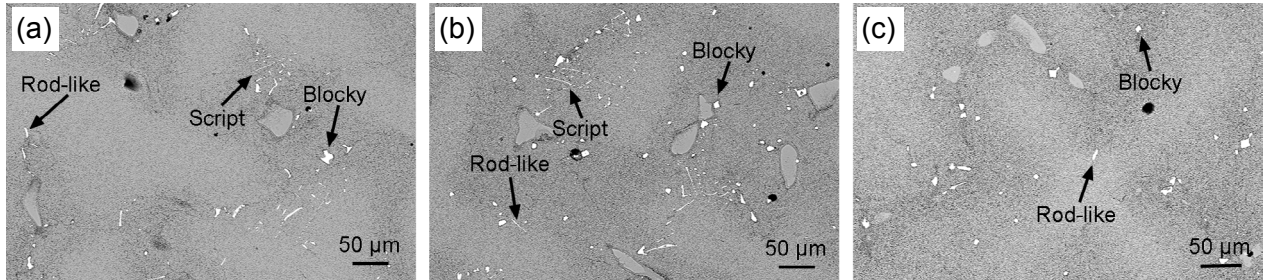


Fig. 6: BSE-SEM images of MC carbides in heat-treated experimental alloys: (a) 0 Hf; (b) 0.2 Hf; (c) 0.4 Hf

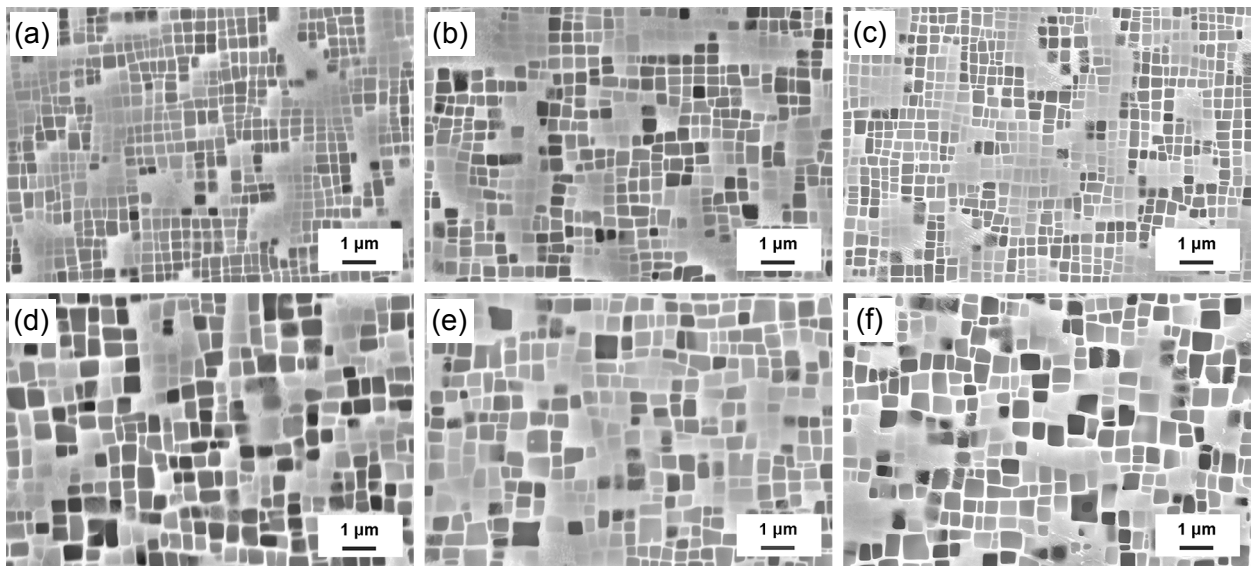


Fig. 7: Typical SEM images of the dendrite core (a, b, and c) and interdendrite regions (d, e, and f) of alloys after heat treatment: (a, d) 0 Hf; (b, e) 0.2 Hf; and (c, f) 0.4 Hf

the size of  $\gamma'$  becomes larger, especially in 0.4 Hf alloy. The results of microstructure characterization of the dendrite core are listed in Table 3. With the increase of Hf content, the volume fraction of  $\gamma'$  and the width of  $\gamma$  matrix channel slightly decreases, while the size of  $\gamma'$  slightly increases.

Table 3: Volume fraction and size of  $\gamma'$  precipitates as well as the width of  $\gamma$  channels in the three experimental alloys after heat treatment

Alloy	Volume fraction of $\gamma'$ phase (%)	Size of $\gamma'$ phase (nm)	Channel width of $\gamma$ phase (nm)
0 Hf	52.2±3.4	372±5	70±8
0.2 Hf	51.0±1.2	381±6	68±5
0.4 Hf	48.9±2.5	394±6	67±3

The elemental partitioning ratios of  $\gamma/\gamma'$  phases obtained from TEM-EDS in the dendrite core of three investigated alloys after heat treatment are shown in Fig. 8. The results show that Mo, Cr, W, and Co are partition in  $\gamma$  phase, but Al, Ti, and Ta are partition in  $\gamma'$  phase in all the three alloys. The partitioning behaviors of Al, Ti, Ta, W, and Co do not change obviously with Hf additions. However, the partitioning behavior of Cr and Mo varies significantly in the three investigated alloys. Their partitioning ratios increase with Hf addition, indicating that Hf promotes the distribution of Cr and Mo to  $\gamma$  phase.

### 3.3 Creep properties

Figure 9(a) illustrates the creep strain curves of the three alloys under 980 °C/200 MPa. Figure 9(b) displays corresponding strain rate as a function of time. All the creep curves exhibit distinctive regions of primary, secondary, and tertiary stage

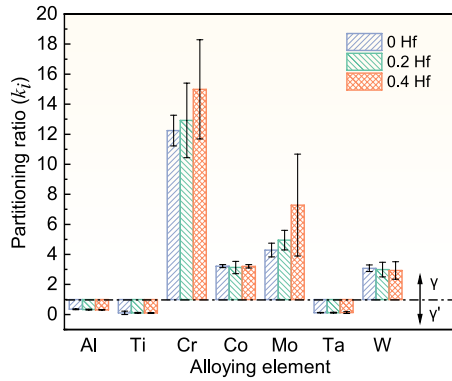


Fig. 8: Elemental partitioning ratios of  $\gamma/\gamma'$  phase in three alloys after heat treatment

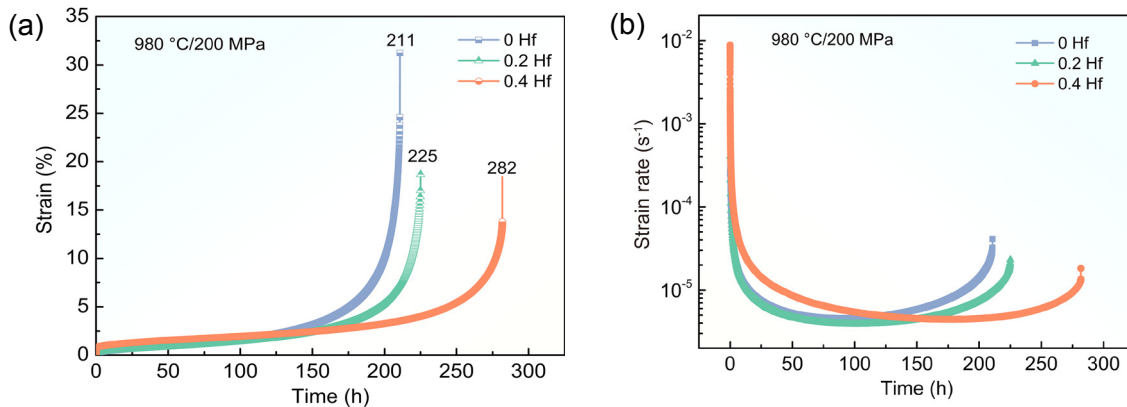


Fig. 9: Creep strain versus time (a) and corresponding strain rate versus time (b) of the three experimental alloys under 980 °C/200 MPa

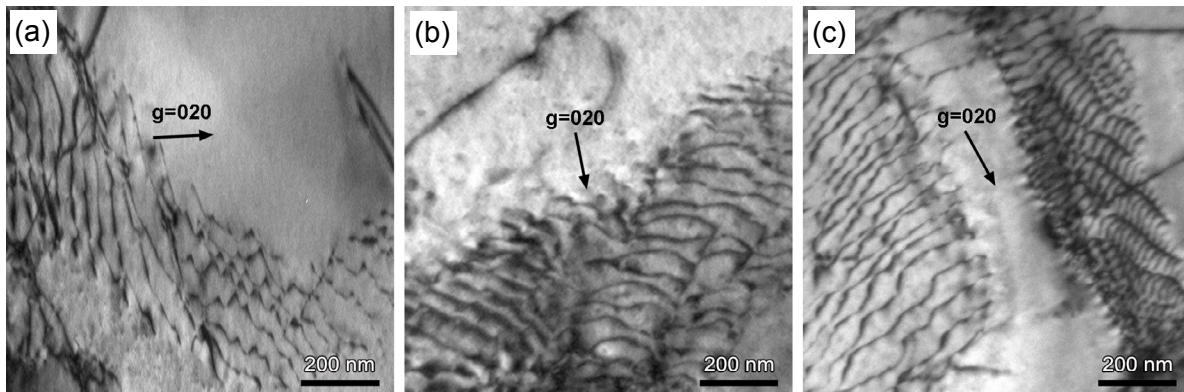


Fig. 10: TEM <200>-type two-beam images from the [001] zone axis of  $\gamma/\gamma'$  interfacial dislocation networks in 0 Hf alloy (a), 0.2 Hf alloy (b), and 0.4 Hf alloy (c) after creep rupture under 980 °C/200 MPa

### 3.5 Creep fracture behavior

The microstructures of the 0 Hf and 0.2 Hf alloys after interrupted creep tests are shown in Fig. 11. Figure 11(a) shows that the script MC carbides fracture during creep, while no fracture are observed around blocky carbides in 0 Hf alloy. This indicates that blocky MC carbides are more effective in suppressing fracture than script MC carbides. Figure 11(b) illustrates that MC carbides debonded from matrix, while the interface of residual eutectics are intact in 0.2 Hf alloy. Obviously, residual eutectics are not the main location for cracks initiation.

Figure 12 illustrates the geometrically necessary dislocation (GND) density around script and blocky MC carbides in the

interrupted creep specimens. The accumulation of plastic deformation around the script MC carbides is apparently larger than that around a blocky carbide.

### 3.4 $\gamma/\gamma'$ interfacial dislocation

The TEM images from the [001] zone axis of typical  $\gamma/\gamma'$  interfacial dislocation network of ruptured specimens are shown in Fig. 10. The average dislocation spacing decreases from 30 nm in 0 Hf to 14 nm in 0.4 Hf alloy. The results indicate that with Hf addition, the  $\gamma/\gamma'$  interfacial dislocation spacing decreases.

interrupted creep specimens. The accumulation of plastic deformation around the script MC carbides is apparently larger than that around a blocky carbide.

## 4 Discussion

Hf elements are usually added to Ni-based SX superalloys to improve the castability and the tolerance of low angle grain boundaries [7, 8]. The present study indicates that, Hf changes the morphology of MC carbides, and affects elemental partitioning ratios, as well as the spacing of  $\gamma/\gamma'$  interfacial dislocation network. An appropriate amount of Hf can improve the creep properties at 980 °C.

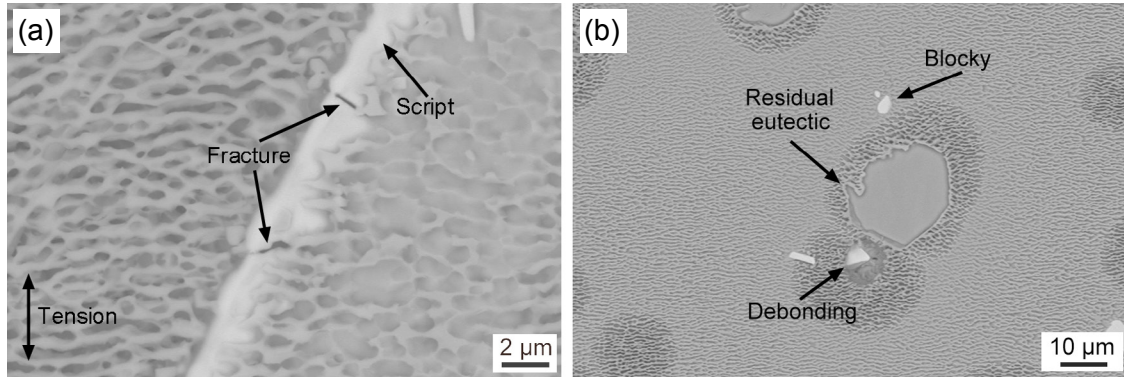


Fig. 11: Microstructures of longitudinal sections of experimental alloys after interrupted creep testing at 980 °C/200 MPa: (a) 0 Hf alloy, 135 h; (b) 0.2 Hf alloy, 145 h

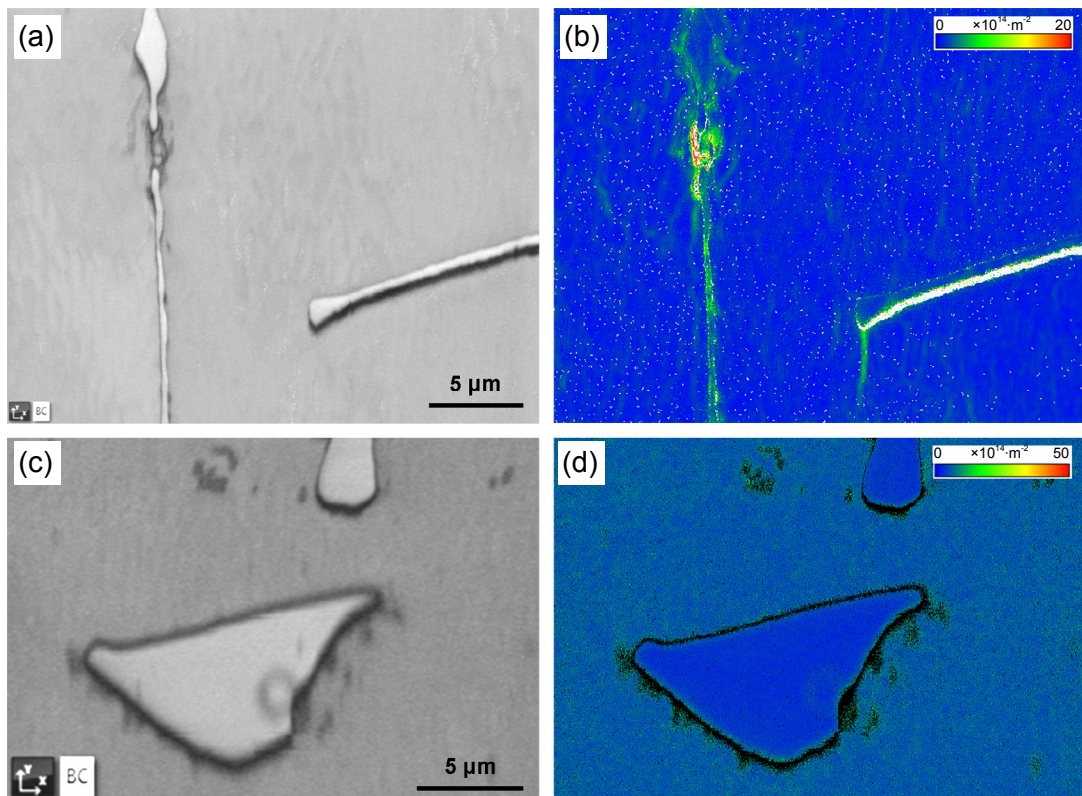


Fig. 12: Backscattered SEM images (a, c) and corresponding geometrically necessary dislocations (GND) density maps (b, d) of MC carbides in an interrupted creep test: (a, b) 0 Hf alloy, 135 h; (c, d) 0.2 Hf alloy, 145 h

#### 4.1 Effect of Hf on carbide morphology

The formation temperature of MC carbides changes with composition, which decreases in the order of HfC>TaC>TiC, according to the calculation obtained from J MatPro, as shown in Fig. 13. Therefore, the carbide formation temperature is thought to be higher in the alloy with a high Hf content<sup>[21]</sup>.

Chen et al.<sup>[22]</sup> reported that octahedron apex direction, i.e. <100> was the preferred carbide growth direction. The morphology of the carbides can be related to their formation temperature, which determines their position in the mushy zone<sup>[23]</sup>. A higher formation temperature means that the carbides appear at higher positions within the solidification process or even above the mushy zone, and therefore their growth is less restricted by the dendrites. Consequently, more

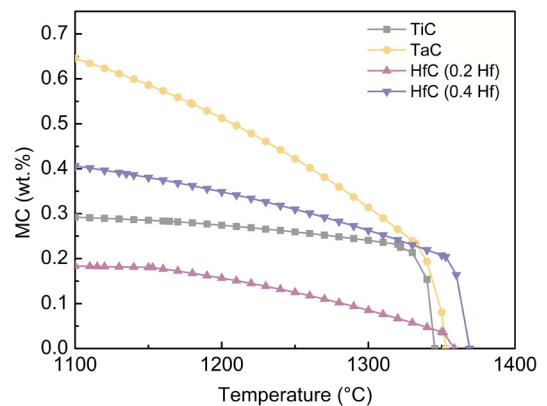


Fig. 13: Formation temperature of MC carbides calculated by J MatPro

carbides with blocky morphology are observed in alloys with a higher Hf content. The carbides with a lower Hf content form at a lower temperature within the liquid channel of the mushy zone. It was reported that the onset of thermal solutal convection was confined to the mushy zone when the  $\gamma$  phase fraction was approximately 63%, and this led to the inhibition of isotropic growth of carbides [24]. In this situation, the arm elongates in the preferred growth direction  $\langle 100 \rangle$  for fcc crystal structure) for easier access to dissolve the carbide forming elements (Hf, Ta, Ti, and C) [25]. Therefore, the preferentially growing along the preferred direction results in a script morphology.

Additionally, with the addition of Hf, the lattice constant of MC carbide increases, leading to the increase of the MC/ $\gamma$  lattice mismatch [17]. The large lattice misfit produces high interface energy, which always intends to form blocky carbides so as to reduce the total interface energy.

## 4.2 Influence of Hf on creep properties

It is easy to understand that the stress concentration leads to the accumulation of local plastic deformation around the script carbides observed during creep (Fig. 12). Obviously, this is detrimental to creep properties. With the addition of Hf, the volume fraction of blocky carbides increases, leading to smaller local plastic deformation and a longer creep rupture life.

The partitioning ratios of Cr and Mo increase with an increase in Hf addition (Fig. 8). This is because Hf segregates into the  $\gamma'$  phase [26]. With the addition of Hf, Cr, and Mo atoms in  $\gamma'$  phase are pushed into  $\gamma$  matrix. Moreover, with the addition of Hf, the fraction of blocky carbides that contain less Cr and Mo increases. This may also result in more Cr and Mo being released into the  $\gamma$  phase, as shown in Fig. 4(b).

Enhanced solid solution strengthening effect is expected by partitioning of Cr and Mo in  $\gamma$  matrix. The change of the partitioning behavior of Cr and Mo also benefits a more negative misfit, and thus a refined interfacial dislocation network. As reported in previous work, a more negative lattice misfit with the finer interfacial dislocation network could hinder the dislocations' movement in the  $\gamma$  matrix and the shearing of dislocations into the  $\gamma'$  phase, leading to a reduction in the minimum creep rate [27-30].

The possible reason for a larger primary creep rate observed in the 0.4 Hf alloy could also be attributed to the morphology of carbides. Blocky carbides in this alloy may have less resistance to the creep deformation comparing to that of the script carbides in the initial stage of creep. Script carbides in the interdendritic region may serve as a strengthening skeleton upon loading, and result in a smaller primary creep rate. The orientation of the creep samples may also show some impact, but is thought to be negligible because the deviation from  $\langle 001 \rangle$  is small ( $2.2^\circ$ ,  $4^\circ$ , and  $6.5^\circ$ , respectively for 0 Hf, 0.2 Hf, and 0.4 Hf alloys).

To sum up, this investigation indicates that the creep properties at high temperatures could be influenced obviously by minor Hf addition. The combination of significant reduction of the number of script carbides and improvement of solid-solution strengthening effect by Cr and Mo contributes to the longer creep rupture life of 0.4 Hf alloy. Meanwhile, residual

eutectics, that are difficult to be removed by solution heat treatment in large blades, do not show significant effect on high temperature creep properties. However, to correlate the amount of fine and blocky carbides and creep properties would be a complex and challenging task in the design of Hf-modified hot corrosion resistant SX superalloys. In such cases, factors such as the heat treatability, cost, and impact of Hf on other properties must also be considered.

## 5 Conclusions

In the present study, the effect of Hf on the as-cast and heat-treated microstructure and creep properties under 980 °C/200 MPa was investigated in three hot corrosion resistant SX superalloys containing various levels of Hf addition (0–0.4wt.%). The conclusions can be summarized as follows:

(1) Hf addition increases the volume fraction of  $\gamma/\gamma'$  eutectics from 2.98% to 4.81% and that of blocky MC carbides from 0.15% to 0.47%, while decreasing the volume fraction of micropores from 0.3% to 0.11% in the as-cast alloys. Hf promotes the transformation of carbide morphology from script to rod-like and finally to blocky, and promotes the distribution of Cr and Mo to  $\gamma$  phase.

(2) Hf addition improves the creep rupture life from 211 h to 282 h at 980 °C/200 MPa of the experimental alloys, but is accompanied by an increase in primary creep rate and a large part of secondary creep rate when Hf content is 0.4wt.%.

(3) Hf addition improves the creep properties by decreasing the volume fraction of script carbides and increasing the solution-strengthening effect.

## Acknowledgments

This work was financially supported by the National Key Research and Development Program of China (No. 2021YFA1600603), the National Science and Technology Major Project (No. J20191-VI-0010-0124), and the National Natural Science Foundation of China (No. 52071219). The authors would also like to thank Ying-ying Shen for his technical assistance on TEM.

## Conflict of interest

The authors declare that they have no conflict of interest.

## References

- [1] Williams J C, Starke E A. Progress in structural materials for aerospace systems. *Acta Materialia*, 2003, 51(19): 5775–5799.
- [2] Pollock T M, Tin S. Nickel-based superalloys for advanced turbine engines: Chemistry, microstructure and properties. *Journal of Propulsion and Power*, 2006, 22(2): 361–374.
- [3] Konter M, Thumann M. Materials and manufacturing of advanced industrial gas turbine components. *Journal of Materials Processing Technology*, 2001, 117: 386–390.
- [4] Meyer M, Dedecke D, Paul U, et al. Undercooling related casting defects in single crystal turbine blades. In: *Superalloys*, TMS, Warrendale, 1996: 471–479.

- [5] Xiao J H, Jiang W G, Han D Y, et al. Effect of the spacial dimensions on solidification defects in rejoined platform of Ni-based single-crystal superalloy castings under different withdrawal rates. *Metallurgical and Materials Transactions: A*, 2021, 52(7): 2936–2947.
- [6] Reed R C. *The superalloys fundamentals and applications*. Cambridge Univeisity Press, Cambridge, 2006: 16.
- [7] Chen Q Z, Jones C N, Knowles D M. The grain boundary microstructures of the base and modified RR 2072 bicrystal superalloys and their effects on the creep properties. *Materials Science and Engineering: A*, 2004, 385(1–2): 402–418.
- [8] Zhao Y S, Zhang J, Luo Y S, et al. Improvement of grain boundary tolerance by minor additions of Hf and B in a second generation single crystal superalloy. *Acta Materialia*, 2019, 176: 109–122.
- [9] Shah D M, Cetel A. Evaluation of PWA1483 for large single crystal IGT blade applications. In: *Superalloys*, TMS, Warrendale, 2000: 295–304.
- [10] Ross E W, O'Hara K S. Rene N4: A first generation single crystal turbine airfoil alloy with improved oxidation resistance, low angle boundary strength and superior long time rupture strength. In: *Superalloys*, TMS, Warrendale, 1996: 19–25.
- [11] Tamaki H, Yoshinari A, Okayama A, et al. Development of a low angle grain boundary resistant single crystal superalloy YH61. In: *Superalloys*, TMS, Warrendale, 2000: 757–766.
- [12] Shi Z X, Li J R, Liu S Z, et al. Effect of Hf content on the microstructures and stress rupture properties of DD6 single crystal superalloy. *Rare Metal Materials and Engineering*, 2010, 39(8): 1334–1338.
- [13] Zhao Y S, Zhang J, Luo Y S, et al. Effects of Hf and B on high temperature low stress creep behavior of a second generation Ni-based single crystal superalloy DD11. *Materials Science and Engineering: A*, 2016, 672: 143–152.
- [14] Chen Q Z, Jones N, Knowles D M. The microstructures of base/modified RR2072 SX superalloys and their effects on creep properties at elevated temperatures. *Acta Materialia*, 2002, 50: 1095–1112.
- [15] Kong Y H, Chen Q Z, Knowles D M. Effects of minor additions on microstructure and creep performance of RR2086 SX superalloys. *Journal of Materials Science*, 2004, 39(23): 6993–7001.
- [16] Zhang H W, Qin X Z, Li X W, et al. Effect of minor additions on the microstructures and stress rupture properties of a directionally solidified Ni-based superalloy. *Materials Science and Engineering: A*, 2018, 711: 303–312.
- [17] Chen Q Z, Jones N, Knowles D M. Effect of alloying chemistry on MC carbide morphology in modified RR2072 and RR2086 SX superalloys. *Scripta Materialia*, 2002, 47(10): 669–675.
- [18] Zhang Y P, Qin J C, Huang Z H, et al. Effect of Hf content on the stress rupture properties of the second-generation single-crystal superalloy with LAB. In: *Proceedings of Chinese Materials Conference 2018, Physics and Engineering of Metallic Materials*, Xiamen China, 2018: 505–514.
- [19] Shi Z X, Li J R, Liu S Z. Effect of Hf on stress rupture properties of DD6 single crystal superalloy after long term aging. *Journal of Iron and Steel Research International*, 2012, 19 (7): 66–70.
- [20] Baldan A. Electron microprobe investigation of lower melting regions in the as-cast structure of DS200+Hf single crystal. *Journal of Materials Science*, 1990, 25: 4341–4348.
- [21] Tan S, Pollock T M. Stabilization of thermosolutal convective instabilities in Ni-based single-crystal superalloys carbide precipitation and rayleigh numbers. *Metallurgical and Materials Transactions: A*, 2003, 34: 1953–1967.
- [22] Chen J, Lee J H, Jo C Y, et al. MC carbide formation in directionally solidified MAR-M247 LC superalloy. *Materials Science and Engineering: A*, 1998, 247: 113–125.
- [23] Cutler E R. Effect of carbon additions and carbide morphology on the microstructure and mechanical properties of nickel-base superalloys. Master's Dissertation, Florida: University of Florida, 2006: 1–124.
- [24] Jia L, Cui H, Yang S F, et al. Effect of carbon addition on microstructure and mechanical properties of a typical hard-to-deform Ni-base superalloy. *Progress in Natural Science Materials International*, 2023, 33(2): 232–243.
- [25] Dadoo A, Boutorabi S M A, Kheirandish S. Effect of titanium carbide concentration on the morphology of MC carbides in pulsed laser surface alloyed AISI H13 tool steel. *Optics and Laser Technology*, 2019, 112: 236–244.
- [26] Ou M Q, Ma Y C, Hou K L, et al. Effect of hafnium content on the microstructural evolution and stress rupture properties of K4750 nickel-based superalloy. *Journal of Alloys and Compounds*, 2022, 916: 165473.
- [27] Zhang J X, Murakumo T, Harada H, et al. Dependence of creep strength on the interfacial dislocations in a fourth generation SC superalloy TMS-138. *Scripta Materialia*, 2003, 48: 287–293.
- [28] Carroll L J, Feng Q, Pollock T M. Interfacial dislocation networks and creep in directional coarsened Ru-containing nickel-base single-crystal superalloys. *Metallurgical and Materials Transactions: A*, 2008, 39(6): 1290–1307.
- [29] Zhang J X, Wang J C, Harada H, et al. The effect of lattice misfit on the dislocation motion in superalloys during high-temperature low-stress creep. *Acta Materialia*, 2005, 53(17): 4623–4633.
- [30] Wang X G, Liu J L, Jin T, et al. Dislocation motion during high-temperature low-stress creep in Ru-free and Ru-containing single-crystal superalloys. *Materials and Design*, 2015, 67: 543–551.